

Critical gravitational collapse with angular momentum

Carsten Gundlach

Mathematical Sciences, University of Southampton, Southampton SO17 1BJ, United Kingdom

Thomas W. Baumgarte

Department of Physics and Astronomy, Bowdoin College, Brunswick, ME 04011, USA

(Dated: 22 September 2016)

We derive a theoretical model of mass and angular momentum scaling in type-II critical collapse with rotation. We focus on the case where the critical solution has precisely one, spherically symmetric, unstable mode. We demonstrate agreement with numerical results for critical collapse of a rotating radiation fluid, which falls into this case.

I. INTRODUCTION

Critical collapse in general relativity refers to phenomena that occur at the threshold, in the space of initial data, between data that lead to black hole formation (collapse) and those that do not. Regular initial data can be classified as supercritical or subcritical according to whether or not they form a black hole. We refer to the boundary between supercritical and subcritical data as the black-hole threshold, or the critical surface. In type-II critical collapse, the black-hole mass formed by supercritical data becomes arbitrarily small as the threshold is approached, and scales as a universal power of distance from this threshold. The exponent in these power laws is referred to as the critical exponent. Critical collapse was first reported in the seminal work of Choptuik [1], who performed numerical time evolutions of a massless scalar field in spherical symmetry. Soon afterwards, similar results were reported for a radiation fluid, i.e. a perfect fluid with the ultra-relativistic equation of state $P = \rho/3$ [2] (where P is the pressure and ρ the total energy density), and for axisymmetric gravitational waves in vacuum [3]. The literature on numerous further numerical experiments as well as theoretical derivations of the scaling laws is reviewed in [4].

In [5], one of us (CG) showed that the spherically symmetric, continuously self-similar critical solution for perfect fluid collapse with the equation of state $P = \kappa\rho$ has only a single ($l = 0$) unstable mode for the range $1/9 < \kappa \lesssim 0.49$, which includes radiation fluids with $\kappa = 1/3$. Based on this, and the more general theory given in [6], CG predicted power-law scaling for the black-hole mass and angular momentum for initial data with small deviations from spherical symmetry, and computed numerical values for the critical exponents.

In [7], the other one of us (TWB), together with Montero, carried out the first critical collapse simulations of a radiation fluid in the absence of spherical symmetry. More recently, we generalized these simulations to study critical collapse with angular momentum [8]. Specifically, we considered a two-parameter family of initial data describing rotating radiation fluids, with one parameter η controlling the strength of the initial data and a second parameter Ω their angular momentum. These simula-

tions confirmed the critical exponents found in [6] and provided evidence for their universality.

In Sec. II we provide a self-contained derivation of the scaling laws in rotating critical collapse, and in Sec. III we demonstrate agreement with the numerical results of [8] for radiation fluids with $\kappa = 1/3$. Sec. IV contains a summary and discussion of our results.

II. SCALING LAWS FOR ROTATING CRITICAL COLLAPSE

Consider an analytic family of regular initial data parameterized by two parameters p and \mathbf{q} . We assume that, if these data evolve to form a black hole, the black-hole mass M and angular momentum \mathbf{J} obey the symmetries

$$M(p, -\mathbf{q}) = M(p, \mathbf{q}), \quad (1a)$$

$$\mathbf{J}(p, -\mathbf{q}) = -\mathbf{J}(p, \mathbf{q}). \quad (1b)$$

A sufficient condition for these two assumptions to hold is that $\mathbf{q} \rightarrow -\mathbf{q}$ corresponds to a spatial reflection of the initial data. The assumption (1b) implies that initial data with $\mathbf{q} = 0$ form a non-spinning black hole, but not that they are necessarily spherically symmetric. In the following, for simplicity of notation, we restrict to axisymmetry, so that q and J become numbers.

The black hole threshold within such a two-parameter family is a curve in the (p, q) -plane that is symmetric under $q \rightarrow -q$. We can fine-tune the initial data to the black hole threshold, in practice by bisection along any smooth 1-parameter family of initial data that crosses it.

The general theory of type-II critical collapse [4] is based on the assumption that the solution first evolves towards an intermediate regime, during which it is approximated by a universal critical solution that contracts in a self-similar fashion. The critical solution has at least one unstable mode, however, which ultimately drives the evolution either towards black-hole formation or dispersal. In the following we discuss these different stages of the time evolution separately.

A. From the initial data to the intermediate self-similar regime

According to our assumption, initial data sufficiently close to the black-hole threshold evolve to an intermediate regime during which the solution Z is given by a critical solution Z_* plus linear perturbations. Here Z denotes a set of first-order in time dynamical variables and (\mathbf{x}, τ) a set of 3+1 coordinates, such that $Z(\mathbf{x}, \tau) = Z(\mathbf{x})$ if and only if the spacetime is continuously self-similar (homothetic).

Variables and coordinates $Z(\mathbf{x}, \tau)$ can be constructed as follows. If we write the physical spacetime metric g_{ab} in the adapted coordinates (\mathbf{x}, τ) as

$$g_{\mu\nu}(\mathbf{x}, \tau) = e^{-2\tau} \bar{g}_{\mu\nu}(\mathbf{x}, \tau), \quad (2)$$

then the spacetime is continuously self-similar with the homothetic vector $\partial/\partial\tau$ if and only if all components of the conformal metric $\bar{g}_{\mu\nu}(\mathbf{x}, \tau)$ are independent of τ . If we now choose the surfaces of constant τ to be space-like, then τ is both a time coordinate and the logarithm of overall spacetime scale. In spherical symmetry or axisymmetry, a natural choice for the remaining coordinates would be a rescaled radius $x = e^\tau r$, where r is, for example, an areal radius, plus two angles. We could then carry out the usual 3+1 split of $\bar{g}_{\mu\nu}$. Assuming for simplicity that the lapse and shift are evolved using first-order in time coordinate conditions, and that the matter is a perfect fluid with the simple linear (ultrarelativistic) equation of state $P = \kappa\rho$, (as is the case for our simulations in [8]), we could choose the variables Z to be the first-order metric variables \bar{g}_{ij} , \bar{K}_{ij} , $\bar{\alpha}$, $\bar{\beta}^i$, the fluid 3-velocity v^i , and $\bar{\rho} := e^{2\tau}\rho$. The initial data $Z(\mathbf{x}, \tau_0)$ for the barred quantities define the solution only up to an overall scale. This scale is given by $e^{-\tau_0}$. (More precisely, it is $Le^{-\tau_0}$, where L is an arbitrary constant of dimension length, in units where $c = G = 1$, but for simplicity of notation we choose units where $L = 1$.) Note that we do not need to use these coordinates in numerical time evolutions.

Using this notation, we can now write the intermediate, approximately self-similar regime as

$$\begin{aligned} Z(\mathbf{x}, \tau) \simeq & Z_*(\mathbf{x}) + P(p, q) e^{\lambda_0\tau} Z_0(\mathbf{x}) \\ & + Q(p, q) e^{\lambda_1\tau} Z_1(\mathbf{x}) \\ & + \text{decaying perturbations.} \end{aligned} \quad (3)$$

Here, $Z_*(\mathbf{x})$ is the critical solution, which, in perfect fluid critical collapse, is both continuously self-similar and spherically symmetric.¹ Z_0 is the unique growing

spherical mode ($l = 0$), and so $\lambda_0 > 0$. The amplitude of this mode, $P(p, q)$, depends on the parameters p and q of the initial data. Z_1 is an $l = 1$ axial mode, namely either the unique growing one (in which case we have $\lambda_1 > 0$), or the least damped one ($\lambda_1 \leq 0$). Its amplitude $Q(p, q)$ again depends on the initial data. We normalise Z_0 and Z_1 later. When there are two growing modes, we single out both in the analysis because they dominate the dynamics. When only Z_0 is growing, we still need to keep track of Z_1 because it is closely linked to black hole angular momentum: Kerr is an axial $l = 1$ perturbation of Schwarzschild to linear order in J/M^2 [6].

We now define the specific moment of time

$$\tau_* := -\frac{1}{\lambda_0} \ln |P|, \quad (4)$$

which we assume to be in the intermediate self-similar regime. At $\tau = \tau_*$, the lengthscale of the solution is then given by

$$e^{-\tau_*} = |P|^{1/\lambda_0}, \quad (5)$$

and, since $|P|e^{\lambda_0\tau_*} = 1$, we have the intermediate Cauchy data

$$\begin{aligned} Z(\mathbf{x}, \tau_*) \simeq & Z_*(\mathbf{x}) \pm Z_0(\mathbf{x}) + \delta Z_1(\mathbf{x}) \\ & + \text{decaying perturbations.} \end{aligned} \quad (6)$$

Here the sign in front of Z_0 is that of P ; it appears because of the absolute value taken in the definition (4). We have also defined

$$\delta := Q|P|^{-\epsilon}, \quad (7)$$

with

$$\epsilon := \frac{\lambda_1}{\lambda_0}. \quad (8)$$

For any 2-parameter family of initial data with parameters (p, q) that obey the symmetries (1) we define the black hole threshold, i.e. the critical curve separating supercritical data from subcritical data, by $(p, q) = (p_*, q_*) = (p_{\text{crit}}(q_*), q_*)$. We also define $p_{*0} := p_{\text{crit}}(0)$, and shall refer to $(p, q) = (p_{*0}, 0)$ as the critical point. From the symmetry (1b), $p_{\text{crit}}(q) = p_{\text{crit}}(-q)$. To fix the coordinate freedom on the space of initial data to first order about the critical point [by linear transformations of p and q that respect (1)], we define the ‘‘reduced parameters’’

$$\bar{p} := C_0(p - p_{*0}), \quad \bar{q} := C_1q, \quad (9)$$

where C_0 and C_1 are family-dependent constants. They will be fixed later.

If $P(p, q)$ and $Q(p, q)$ are analytic (because the initial data are analytic), we can expand them in powers of \bar{p} and \bar{q} . By definition P vanishes at the critical point $\bar{p} = \bar{q} = 0$. Moreover, from the symmetry (1a), P must be even in \bar{q} . This suggests that we treat \bar{p} and \bar{q}^2 as

¹ For scalar fields, Z_* is discretely self-similar and spherically symmetric, and for vacuum gravity it is believed to be discretely self-similar and axisymmetric. These symmetries are more complicated on a technical level, but the basic ideas presented here are unchanged.

the same order of smallness when expanding about the critical point. From the symmetry (1b), Q must be odd in \bar{q} . We may therefore expand

$$P = \bar{p} - K\bar{q}^2 + \mathcal{O}(\bar{p}^2, \bar{p}\bar{q}^2, \bar{q}^4), \quad (10a)$$

$$Q = \bar{q} + \mathcal{O}(\bar{q}^3, \bar{p}\bar{q}), \quad (10b)$$

where we have now fixed the family-dependent constants C_0 and C_1 so that the leading-order terms in these expansions have coefficients of unity.

The coefficient K , and the coefficients of the higher-order terms that we have not written out here, also depend on the two-parameter family of initial data because they depend on the nonlinear and non-universal evolution from generic initial data to the universal intermediate regime (3). We have inserted the minus sign in (10a) as we anticipate that K will then be positive: spin should resist collapse. Since the critical surface corresponds to $P = 0$, the expansion (10a) also implies that, to leading order, the critical surface forms a parabola in the (p, q) -plane.

B. From the intermediate self-similar regime to the final black hole

The key observation for scaling is the following. As discussed above, initial data sufficiently close to the black-hole threshold pass through an intermediate self-similar phase. During this phase, we can identify the intermediate Cauchy data (6) at $\tau = \tau_*$. These constitute two universal 1-parameter families of scale-invariant intermediate initial data, parameterised by the sign \pm of P and the parameter δ . The scale-invariant data are completed by the overall length scale $e^{-\tau_*}$.

Because the evolution equations are scale-invariant $e^{-\tau_*}$, translates into an overall length and time scale of the solution at all subsequent times. This means that if a feature of the subsequent spacetime evolution has dimension L^n (where L denotes length, in units where $c = G = 1$), then this feature must be proportional to $e^{-n\tau_*}$.

In particular, M must be proportional to the overall scale $e^{-\tau_*} = |P|^{1/\lambda_0}$ of the Cauchy data (6). Moreover, the constant of proportionality can depend only on the sign \pm of P and the dimensionless number δ . We may therefore express it in terms of two functions $F_M^\pm(\delta)$. Similarly, J must be proportional to $e^{-2\tau_*} = |P|^{2/\lambda_0}$, and again the constant of proportionality can be expressed in terms of two functions of $F_J^\pm(\delta)$. With

$$\gamma_M := \frac{1}{\lambda_0} \quad (11)$$

we therefore have [9]

$$M(p, q) \simeq |P|^{\gamma_M} F_M^\pm(\delta), \quad (12a)$$

$$J(p, q) \simeq |P|^{2\gamma_M} F_J^\pm(\delta). \quad (12b)$$

We note that the dimensionless quantity J/M^2 can only depend on the sign \pm and δ . Numerical evidence also shows that collapse actually happens only for $P > 0$, and so in the following we ignore the functions $F_{M,J}^-$, and write $F_{M,J}$ short for $F_{M,J}^+$.

Because of the symmetries (1), $F_M(\delta)$ is even in δ and $F_J(\delta)$ is odd. We can now normalize Z_0 and Z_1 in such a way that that, to leading order, as $\delta \rightarrow 0$, we have

$$F_M(\delta) = 1 + \mathcal{O}(\delta^2), \quad F_J(\delta) = \delta + \mathcal{O}(\delta^3). \quad (13)$$

In particular, Eqs. (12) then imply that

$$J/M^2 = \delta + \mathcal{O}(\delta^3). \quad (14)$$

Inserting the leading-order expressions (13) together with the definitions (7) and (8) into (12) yields

$$M \simeq P^{\gamma_M}, \quad (15a)$$

$$J \simeq P^{\gamma_J} Q, \quad (15b)$$

where we have also defined

$$\gamma_J := \frac{2 - \lambda_1}{\lambda_0}. \quad (16)$$

In geometric terms, P and Q are locally smooth scalar functions on the manifold of smooth initial data, such that $P = 0$ gives the critical surface, and M and J given by (15) are non-smooth at the critical surface precisely because of the non-integer powers γ_M and γ_J . A related observation is that the power-law scalings of M and J at the collapse threshold show the same powers for any 1-parameter family of initial data that crosses the threshold, independently of the angle at which the threshold is crossed (compare Table I in [8]). If we further use the lowest-order approximations for P and Q , Eqs. (10), we obtain

$$M \simeq (\bar{p} - K\bar{q}^2)^{\gamma_M}, \quad (17a)$$

$$J \simeq (\bar{p} - K\bar{q}^2)^{\gamma_J} \bar{q}. \quad (17b)$$

Whether or not the leading-order expressions (13) are an adequate approximation for the scaling functions $F_{J,M}$ depends on whether the critical solution has one or two growing modes. In the case of one growing mode, Eq. (8) gives $\epsilon < 0$ and so from (7) $\delta \rightarrow 0$ as the black-hole threshold $P = 0$ is approached. In the case of two growing modes, however, we have $\epsilon > 0$, so that we expect large values of δ to be explored close to the black-hole threshold.

III. COMPARISON WITH NUMERICAL EXPERIMENTS

The expressions (17) are the main result of this paper for the case where the critical solution has only one growing mode. In the following we compare these predictions with results from numerical time evolutions for rotating radiation fluids, i.e. a perfect fluid with equation of state $P = \kappa\rho$ and $\kappa = 1/3$, for which there is only a single growing mode.

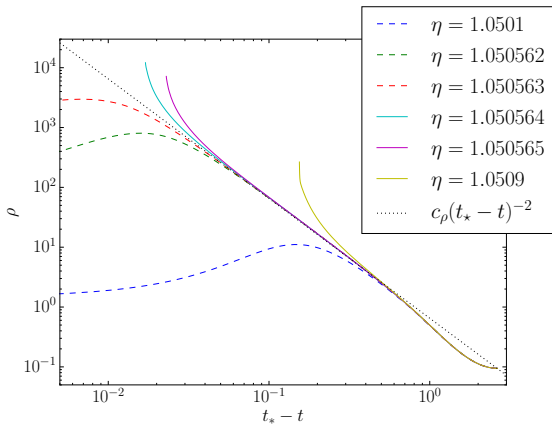


FIG. 1. The central density ρ versus $t_* - t$ for several evolutions with $\Omega = 0.3$. Here t is the proper time as measured by an observer at the center, and t_* is the accumulation time. Supercritical evolutions are marked by solid lines, and subcritical evolutions by dashed lines. The dotted line marks the expression (18) with $c_\rho = 0.65$ and $t_* = 2.6395$ for the critical solution.

A. Numerical setup

We consider the 2-parameter family of initial data previously presented in [8]. Specifically, the initial density distribution ρ is a Gaussian. The overall strength of this density distribution is parametrized by η , and its angular momentum scales with Ω (see Eqs. (6) and (7) in [8]). For $\Omega = 0$ our initial data reduce to those considered in [2]. The parameters η and Ω are instances of the generic parameters p and q in Sect. II. We evolve these data with a code that has been described in [7, 12, 13]. Briefly summarized, we solve the Baumgarte-Shapiro-Shibata-Nakamura formulation of Einstein's equations [14–16] in spherical polar coordinates, using moving-puncture gauge conditions. Details of our numerical specifications can be found in [7, 8].

For initial data that form a black hole we locate a marginally outermost trapped surface, or apparent horizon, using the technique described in [17], and measure its irreducible mass M_{irr} and angular momentum J as in [18]. Both mass and angular momentum increase a little after an apparent horizon is first formed, as the black hole accretes some more material from the surrounding fluid, but they soon settle down to equilibrium values. Assuming that the new black hole is a Kerr black hole, we then compute the Kerr mass $M = M_{\text{irr}} (1 + (J/M_{\text{irr}}^2)^2/4)^{1/2}$ from the equilibrium values of M_{irr} and J . Note that our theoretical derivation of the scaling laws applies equally to M_{irr} and M .

B. Self-similarity

We start by presenting evidence of the underlying assumption of Sect. II, namely that sufficiently close to the black-hole threshold the evolution passes through an intermediate self-similar phase. The evolution during the self-similar phase is governed by only one length-scale. On dimensional grounds the density ρ at the center of symmetry must therefore scale with

$$\rho \simeq c_\rho (t_* - t)^{-2}, \quad (18)$$

where t is the proper time measured by an observer at the center and t_* is the accumulation time of the self-similar solution.

In Fig. 1 we plot ρ versus $t_* - t$ for several members of our family initial data with $\Omega = 0.3$, for which the critical value of η is approximately $\eta_* \simeq 1.0505635$. We include (18) with $c_\rho = 0.65$ and $t_* = 2.6395$ as a fit for the critical solution. All evolutions start in the lower right, and evolve towards the top left. By coincidence, the evolutions start from a point that is close to the dotted line marking the critical solution, but then move away before joining it for real at $t_* - t \simeq 0.5$. After that, evolutions with initial data closer to the threshold remain close to the critical solution for a longer time. In Fig. 1 solid lines mark supercritical evolutions, for which the density ultimately diverges as a black hole is formed, while dashed lines mark subcritical evolutions, for which the density ultimately drops to zero as the fluid disperses to infinity. The evolutions for $\eta = 1.050563$ and 1.050564 bracket the critical solution, and follow the central density as given by (18) over more than two orders of magnitude. However, even for relatively small deviations of η from the critical value, e.g. $\eta = 1.0501$ or 1.0509 in Fig. 1, the solution does not appear to go through a phase of self-similar contraction at all.

C. Power-law scalings

We start our analysis by considering the same 1-parameter families of data that we previously considered in [8], namely sequences for $\Omega = 0, 0.05, 0.1$ and 0.3 , as well as for $\eta = 1.02, 1.035$ and 1.0505 . All families cross the critical curve; locating these intersections provides points (η_*, Ω_*) on the collapse threshold. Our initial observation is that the location of these six points is well approximated by a parabola, as expected from (10a); see Fig. 1 of [8].

For supercritical data we can plot the logarithm of the black-hole masses M and angular momenta J versus the logarithm of the distance from the critical parameter (see Fig. 2 in [8]). Measuring the slope of the resulting straight lines then provides a numerical estimate of the critical exponents γ_M and γ_J . Numerical data can be found in Table I of [8]. For all sequences considered the numerical values are within a few percent of the analyti-

cal values

$$\gamma_M \simeq 0.3558, \quad \gamma_J = \frac{5}{2}\gamma_M \simeq 0.8895 \quad (19)$$

for $\kappa = 1/3$, as computed by [11] and [5], respectively. The fact that these exponents are independent of where and at what angle the sequence crosses the critical curve is a consequence of the scaling laws derived in Sect. II.

Before the predictions (17) can be compared with the numerical data, including all constant factors, we need to determine the family-dependent parameters η_{*0} , C_0 , C_1 in (9) and K in (10a). We first consider the $\Omega = 0$ sequence, for which (17a) reduces to

$$M \simeq \bar{\eta}^{\gamma_M} = C_0^{\gamma_M} (\eta - \eta_{*0})^{\gamma_M}. \quad (20)$$

Fitting this expression to numerical data then yields the parameters $\eta_{*0} = 1.0183772$ (in agreement with [2]) and $C_0 \simeq 0.28$. Fitting to one of the rotating families, for example the $\Omega = 0.05$ sequence, then yields $C_1 \simeq 4.5$ in a similar fashion. Finally, we insert (9) together with the now known coefficients C_0 and C_1 into (10a), set $P = 0$, and fit the resulting relation between η and Ω to the parabola describing the critical curve (η_*, Ω_*) to obtain $K \simeq 0.0046$. We will use these parameters in all of the following plots, which makes them heavily overdetermined.

In Figs. 2 and 3 we plot the theoretical predictions for black-hole masses M and angular momenta J in our two-dimensional parameter space. Specifically, we plot M and J as functions of η and Ω as given by (17), based on the parameters determined above. Fig. 2 contains the data already used in [8], while Fig. 3 contains additional data further away from the critical point. Fig. 2 already suggests good agreement between the theoretical predictions and the numerical data not too far from the critical point, but for a clearer quantitative comparison between model and data we also plot 1-parameter families of either constant Ω or η .

For 1-parameter families at constant $\bar{\Omega} = \bar{\Omega}_*$ (which appear as vertical lines in Fig. 1 of [8]) the scaling laws (17) can be written as

$$M \simeq (\bar{\eta} - \bar{\eta}_*)^{\gamma_M}, \quad (21a)$$

$$J \simeq (\bar{\eta} - \bar{\eta}_*)^{\gamma_J} \bar{\Omega}_*, \quad (21b)$$

where we have used $\bar{\eta}_* = K\bar{\Omega}_*^2$. Inserting the expressions (9) for the reduced parameters we may then define the dimensionless expressions

$$M_\Omega := \frac{M}{(C_0\eta_*)^{\gamma_M}} \simeq \left(\frac{\eta}{\eta_*} - 1 \right)^{\gamma_M}, \quad (22a)$$

$$J_\Omega := \frac{J}{C_1\Omega_*(C_0\eta_*)^{\gamma_J}} \simeq \left(\frac{\eta}{\eta_*} - 1 \right)^{\gamma_J} \quad (22b)$$

for sequences of constant Ω .

Similarly, for 1-parameter families at constant $\bar{\eta} = \bar{\eta}_*$ (which appear as horizontal lines in Fig. 1 of [8]) the

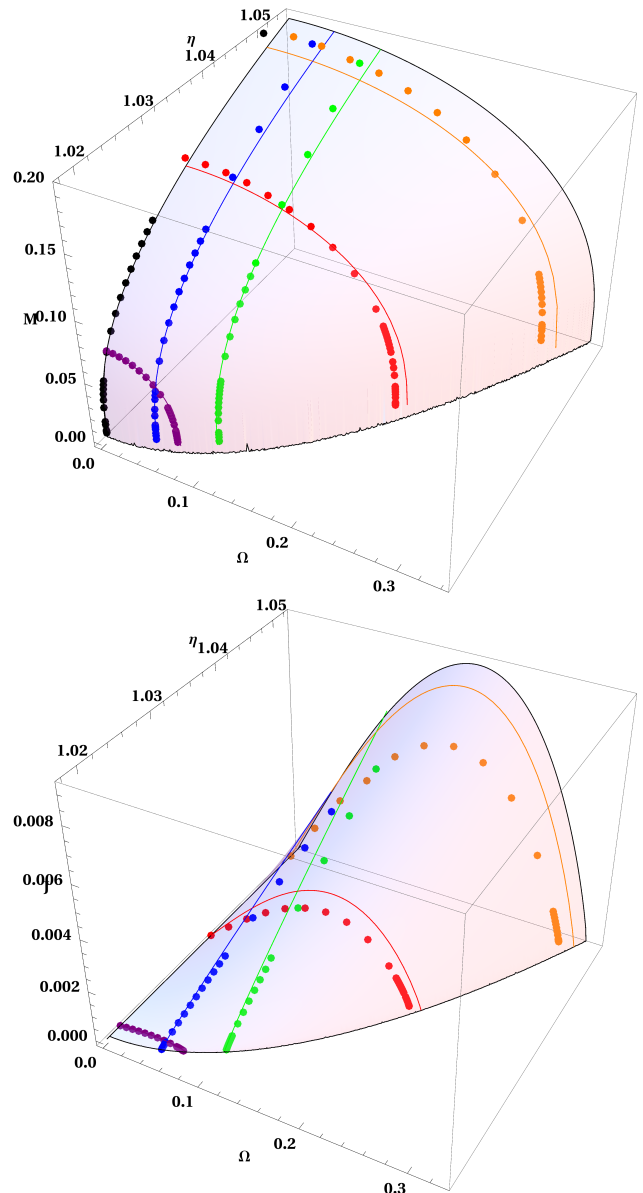


FIG. 2. The theoretical predictions (17) (continuous surface and curves) for black-hole masses M (top) and angular momenta J (bottom), together with numerical data from six 1-parameter families for $\Omega = 0, 0.05$ and 0.1 (black, blue, green) and $\eta = 1.02, 1.035$ and 1.0505 (purple, red, orange).

scaling laws (17) can be written as

$$M \simeq \left[\bar{\eta}_* \left(1 - \frac{\bar{\Omega}^2}{\bar{\Omega}_*^2} \right) \right]^{\gamma_M}, \quad (23a)$$

$$J \simeq \left[\bar{\eta}_* \left(1 - \frac{\bar{\Omega}^2}{\bar{\Omega}_*^2} \right) \right]^{\gamma_J} \bar{\Omega}. \quad (23b)$$

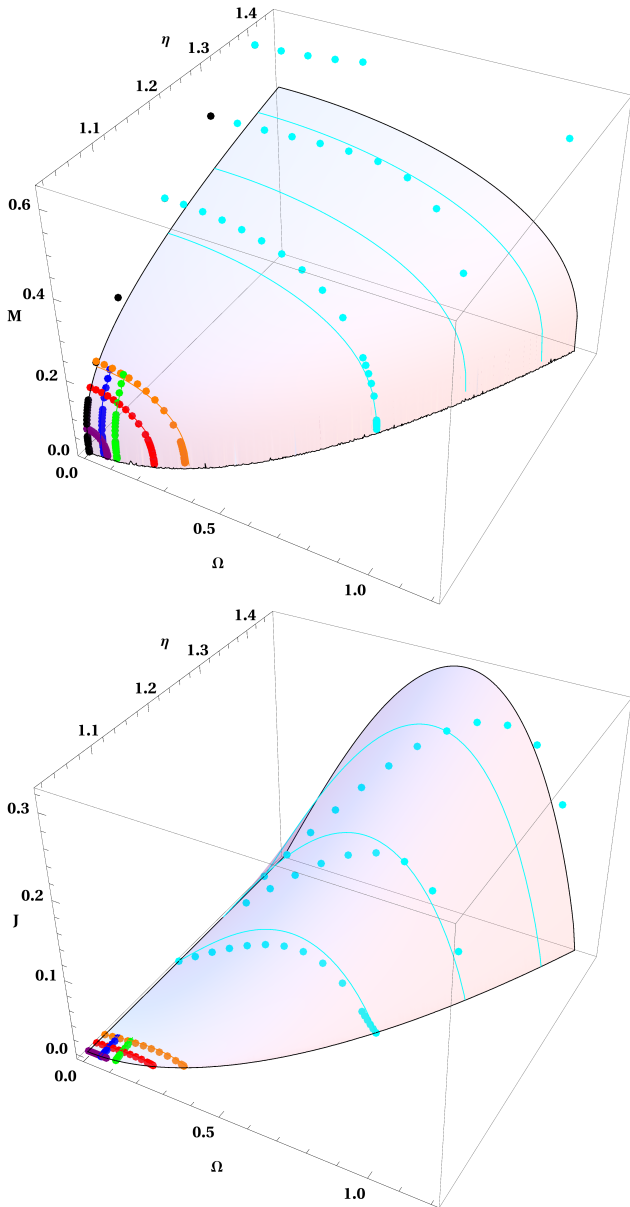


FIG. 3. A zoom-out from the previous figure, showing the previous families of initial data, and in addition $\eta = 1.2, 1.3$ and 1.4 (all in cyan). These additional data show increasing deviations from the theoretical model further away from the critical point, as is in fact required to maintain $|J|/M^2 < 1$.

For sequences of constant η we then define

$$M_\eta := \frac{M}{M_{\max}} \simeq \left(1 - \frac{\Omega^2}{\Omega_*^2}\right)^{\gamma_M}, \quad (24a)$$

$$J_\eta := \frac{J}{J_{\max}} \simeq \frac{1}{C_J} \left(1 - \frac{\Omega^2}{\Omega_*^2}\right)^{\gamma_J} \frac{\Omega}{\Omega_*} \quad (24b)$$

(these are Eqs. (9) and (10) of [8]), where we have abbreviated

$$M_{\max} = [C_0(\eta_* - \eta_{*0})]^{\gamma_M}, \quad (25a)$$

$$J_{\max} = C_J C_1 \Omega_* [C_0(\eta_* - \eta_{*0})]^{\gamma_J}. \quad (25b)$$

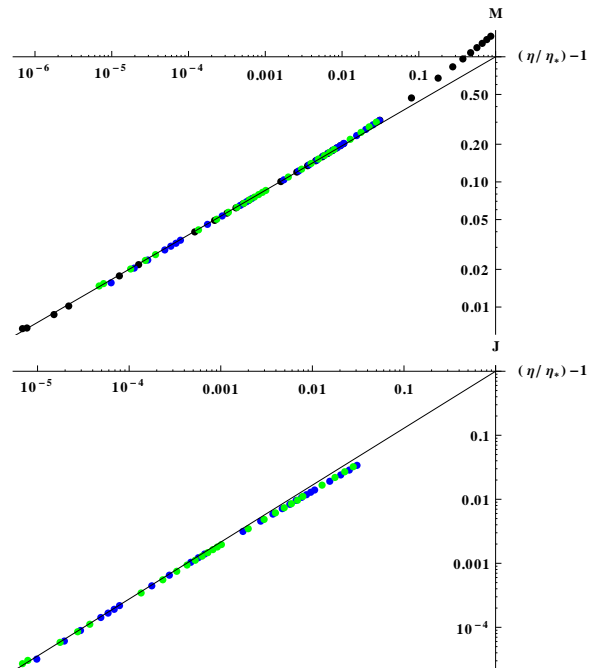


FIG. 4. Verification of (22a) for M (top) and (22b) for J (bottom). The continuous curves are the analytic expressions on the right-hand sides of these equations, plotted against $(\eta/\eta_*) - 1$. The dots are numerical values for the left-hand sides, for the three 1-parameter families of initial data at constant $\Omega = 0, 0.05, 0.1$ (black, blue, green, as for the same data in Fig. 2). The critical surface is at an infinite distance to the bottom left in this log-log plot. There is obviously no J plot for the $\Omega = 0$ family.

To leading order, these quantities are the maximum mass and angular momentum along the sequence of constant η , and $C_J \simeq 0.4025$ is the maximum of $x(1-x^2)^{\gamma_J}$ on the interval $[0, 1]$.

In Fig. 4 we plot the masses and angular momenta of black holes formed from supercritical data in families of constant Ω , and in Fig. 5 for families of constant η . In these graphs, the solid lines represent the right-hand sides of Eqs. (22) and (24), while the points mark the numerical data, rescaled as on the left-hand sides of (22) and (24). These rescaling factors include the parameters C_0, C_1 and η_{*0} as determined above for the entire two-parameter family of initial data; i.e. these parameters are not fitted separately to the individual 1-parameter families shown in the figures. In addition, the rescaling factors include the critical values η_* or Ω_* for each 1-parameter family. In principle, these could be computed by setting $P = 0$ in (10a), which yields

$$C_0(\eta_* - \eta_{*0}) \simeq K(C_1 \Omega_*)^2. \quad (26)$$

Using this expression would result in a small error in the critical parameters but a diverging *relative* error for M and J at the collapse threshold, thus hiding the physically correct scaling law. This is already familiar elsewhere in the numerical study of critical phenomena: numerical

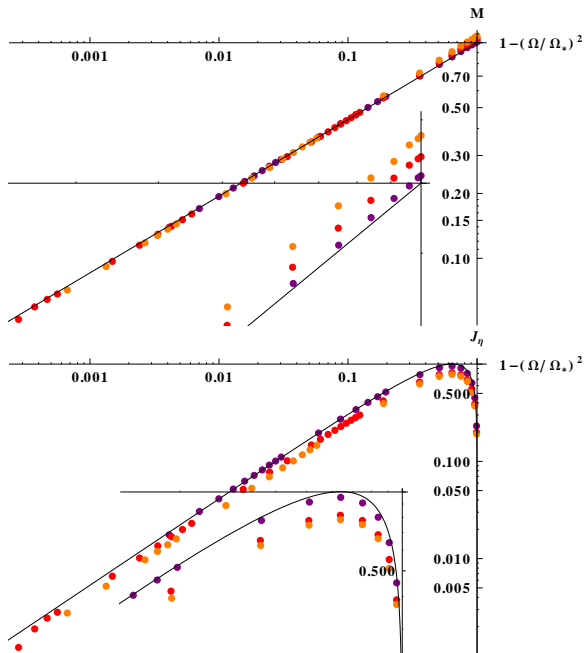


FIG. 5. Verification of (24a) for M (top) and (24b) for J (bottom). The continuous curves are the analytic expressions on the right-hand sides of these equations, plotted against $1 - (\Omega/\Omega_*)^2$. The dots are numerical values for the left-hand sides, for the three 1-parameter families of initial data at constant $\eta = 1.02, 0.1035, 1.0505$ (purple, red, orange, as for the same data in Fig. 2). The critical surface is at an infinite distance to the bottom left in this log-log plot. $\Omega = 0$ is at the right edge of the plot, and the fall-off there represents $J \sim \Omega$ for small Ω in this log-log plot.

values of, say, a critical exponent or the critical parameter of a 1-parameter family converge to a continuum limit with increasing numerical resolution, but data at a given resolution will show critical scaling only for the critical parameters obtained for that resolution, rather than higher-resolution values. For a similar reason, we fit η_* or Ω_* for the individual 1-parameter families, rather than using (26), so that the data reveal critical scaling even close to the black-hole threshold.

For data sufficiently close to the critical point, there is good agreement between the prediction and numerical values. This is shown in Fig. 2. The differences increase further away from the critical point, where we expect increasing deviations between the leading-order scaling laws and non-linear numerical evolutions. In particular, the maxima of $|\delta|$ with respect to $\bar{\Omega}$ at constant $\bar{\eta}$ lie on the parabola

$$\frac{\partial}{\partial \bar{\Omega}} \delta(\bar{\eta}, \bar{\Omega}) = 0 \quad \Rightarrow \quad \bar{\eta} \simeq (1 - 2\epsilon)K\bar{\Omega}^2. \quad (27)$$

Along this curve, parameterised by $\bar{\eta}$, our model predicts

$$\max_{\bar{\Omega}} \frac{J}{M^2}(\bar{\eta}, \bar{\Omega}) \simeq K^{-\frac{1}{2}}(-2\epsilon)^{-\epsilon}(1 - 2\epsilon)^{\epsilon - \frac{1}{2}}\bar{\eta}^{\frac{1}{2} - \epsilon}, \quad (28)$$

which increases monotonically with $\bar{\eta}$. Hence we ex-

pect our model to break down well before it predicts $|J|/M^2 > 1$. Indeed, we find that further away from the critical point the numerically found masses are larger than predicted, and the angular momenta smaller than predicted, such that J/M^2 increases but never goes beyond unity. These observations are demonstrated in Fig. 3.

We would like to emphasize a difference between Figs. 4 and 5 and the scaling plots of [8]. In Fig. 2 of [8] we fitted power-laws to individual 1-parameter families, whereas here we compare the numerical data with predictions for the entire two-parameter family, given the constants C_0, C_1 and η_{*0} . Similarly, for Fig. 4 of [8], which shows the same data as Fig. 5 here, we computed M_{\max} and J_{\max} in (24) from the numerical data (which did not require knowledge of the constants C_0, C_1 and η_{*0}), whereas here we compute M_{\max} and J_{\max} from (25), using the constants C_0, C_1 and η_{*0} . The agreement found here is therefore a more stringent comparison between theoretical predictions and numerical data than that presented in [8].

IV. SUMMARY AND DISCUSSION

We have extended arguments previously presented in [5, 6, 9] to derive new closed-form scaling laws for critical collapse with angular momentum. The main result, Eq. (12), in principle involves scaling functions $F_{M,J}$ that need to be determined numerically, but adopting the lowest-order expansions (13) of these scaling functions yields the predictions (17). We have compared these predictions with numerical simulations for rotating radiation fluids and find excellent agreement. We believe that the agreement between theory and numerics for the mass and angular momentum scaling, even so far from critical collapse that there is no clear sign of an intermediate self-similar regime, is another example of the “unreasonable effectiveness of perturbation theory”, similar to post-Newtonian approximations [19] and the close-limit approximation [20] for binary black hole mergers.

This paper also demonstrates the necessary interplay between theory and numerical experiment in critical collapse. In the previous treatment [5, 6, 9] CG implicitly truncated the expansion (10a) as $P = \bar{p}$, which renders the black-hole threshold as a straight line. The numerical results of [8] showed that the resulting picture is qualitatively incorrect. In hindsight, $\mathcal{O}(\bar{p}) = \mathcal{O}(\bar{q}^2)$, so that the consistent lowest-order truncation of the coefficients P and Q is (10), and the black-hole threshold is a parabola. For the case of one unstable mode, CG correctly predicted the scaling behaviour (15) for small \bar{q} , but by implicitly setting $K = 0$ (in the notation of this paper) he missed the equally interesting behavior of (17) for finite \bar{q} , in particular (23). The formal prediction of nontrivial universal scaling functions (12) for the mass and angular momentum has not changed, but δ is now given in terms of P and Q , not \bar{p} and \bar{q} , with the lowest-order consistent

truncation given by Eq. (10).²

In Sect. III we compared the theory with numerical results the perfect fluids with the equation of state $P = \kappa\rho$ where $\kappa = 1/3$ (the radiation fluid). As discussed in the Introduction, for $1/9 < \kappa \lesssim 0.49$ the critical solution has only one unstable mode, so that $\epsilon < 0$ in particular for $\kappa = 1/3$. Eq. (7) then implies $\delta \rightarrow 0$ as the black-hole threshold $P = 0$ is approached, which, by (14), implies $J/M^2 \rightarrow 0$, in agreement with our numerical findings.

It is precisely the fact that $\delta \rightarrow 0$ at the black-hole threshold that allows us to use the simple expansions (13) for the scaling functions in (15). For $\kappa < 1/9$, on the other hand, we expect two unstable modes, so that $\epsilon > 0$, in which case (7) suggests that δ grows without bound as $P \rightarrow 0$. In this case, therefore, use of the expansions (13) can no longer be justified. We plan to explore this regime in the future.

We would like to stress that the derivation of (17) relies on at least four logically independent perturbation approximations: (i) Sufficiently near the collapse threshold the time evolution actually goes through a phase where it can be described by the critical solution plus linear perturbations. (ii) In at least part of this phase, all decaying linear perturbations, except possibly for Z_1 , can be neglected. (iii) The scaling functions can be approximated by their leading orders (13). (iv) The amplitudes P and Q can be approximated by their leading orders (10).

It is hard to know which of these approximations causes the most significant deviations from (17) as we move away from the critical point. One might consider adding higher powers of \bar{p} and \bar{q} to the expressions for P and Q as indicated in (10) to control (iv). However,

as $M(p, q)$ and $J(p, q)$ are smooth functions away from the critical surface, we can always make our model fit the data precisely by fitting $P(p, q)$ and $Q(p, q)$, and so this fit has no additional predictive power.

One might also consider extending (13) to a power series in δ to control (iii). However, we can already fit the model to the numerics perfectly by fitting P and Q , even if we set $F_M = 1$ and $F_J = \delta$, and so we cannot determine these universal functions by such a fit. They could, however, be defined directly by the time evolution of the two 1-parameter family of universal intermediate initial data (6). The scaling functions will play a non-trivial role when there are two unstable modes, as $\delta \rightarrow 0$ is then still realised as $\bar{q} \rightarrow 0$ but $\delta \rightarrow \infty$ is realised as $\bar{q} \rightarrow \bar{q}_*(\bar{p})$.

We note in closing that Aguilar-Martinez [21] has presented preliminary numerical results for the critical collapse, in *Newtonian* gravity, of an axisymmetric rotating fluid with equation of state $P \propto \rho_0^\Gamma$ (where ρ_0 is the rest mass density) with $\Gamma = 10^{-5}$. The critical solution appears to have two unstable modes in this case. Aguilar-Martinez gives theoretical values of $\lambda_0 \simeq 9.4643$ and $\lambda_1 = 1/3$, implying $\epsilon \simeq 0.3522$. The black-hole threshold found in his simulations appears to be well approximated by a parabola. Interestingly, $M(p, q)$ and $J(p, q)$ also approach zero at the black-hole threshold even though there are two unstable modes. It will be interesting to compare the case of two unstable modes in general relativity.

ACKNOWLEDGMENTS

This work was supported in part by NSF grant PHY-1402780 to Bowdoin College.

-
- [1] M. W. Choptuik Phys. Rev. Lett. **70**, 9 (1993).
 - [2] C. R. Evans and J. S. Coleman, Phys. Rev. Lett. **72**, 1782 (1994).
 - [3] A. M. Abrahams and C. R. Evans, Phys. Rev. Lett. **70**, 2980 (1993).
 - [4] C. Gundlach and J. M. Martín-García, Living Rev. Relativity, **2007-05** (2007).
 - [5] C. Gundlach, Phys. Rev. D **65**, 084021 (2002).
 - [6] C. Gundlach, Phys. Rev. D **57**, R7080 (1998).
 - [7] T. W. Baumgarte and P. J. Montero, Phys. Rev. D **92**, 124065 (2015).
 - [8] T. W. Baumgarte and C. Gundlach, Phys. Rev. Lett. **116**, 221103 (2016).
 - [9] C. Gundlach, Phys. Rev. D **65**, 064019 (2002).
 - [10] T. Koike, T. Hara and S. Adachi, Phys. Rev. Lett. **74**, 5170 (1995).
 - [11] D. Maison, Phys. Lett. B **366**, 82 (1996).
 - [12] T. W. Baumgarte, P. J. Montero, I. Cordero-Carrión and E. Müller, Phys. Rev. D **87**, 044026 (2013).
 - [13] T. W. Baumgarte, P. J. Montero and E. Müller, Phys. Rev. D **91**, 064035 (2015).
 - [14] T. Nakamura, K. Oohara and Y. Kojima, Prog. Theor. Phys. Suppl. **90**, 1 (1987).
 - [15] M. Shibata and T. Nakamura, Phys. Rev. D **52**, 5428 (1995).
 - [16] T. W. Baumgarte and S. L. Shapiro, Phys. Rev. D **59**, 024007 (1998).
 - [17] M. Shibata and K. Uryū, Phys. Rev. D **62**, 087501 (2000).
 - [18] O. Dreyer, B. Krishnan, D. Shoemaker and E. Schnetter, Phys. Rev. D **67**, 024018 (2003).
 - [19] C. M. Will, PNAS **108**, 5938 (2011).
 - [20] R. H. Price and J. Pullin, Phys. Rev. Lett. **72**, 3297 (1994).
 - [21] S. Aguilar-Martinez, “Critical collapse of Newtonian fluids”, PhD thesis, University of British Columbia, draft version dated August 2015 and communicated privately.

² The similarity between our Fig. 2 and Fig. 2 of [9] is, unfortu-

nately, accidental.